

High accuracy determination of photoelectric cross sections, X-ray absorption fine structure and nanostructure analysis of zinc selenide using the X-ray extended range technique

Daniel Sier,^a Geoffrey P. Cousland,^a Ryan M. Trevorah,^a Ruwini S. K. Ekanayake,^a Chanh Q. Tran,^b James R. Hester^c and Christopher T. Chantler^{a*}

Received 2 June 2020

Accepted 21 July 2020

Edited by S. M. Heald, Argonne National Laboratory, USA

Keywords: ZnSe; XAFS; XERT; K-edges; 0.1% accuracy.

Supporting information: this article has supporting information at journals.iucr.org/s

^aSchool of Physics, University of Melbourne, Australia, ^bLa Trobe University, Australia, and ^cAustralian Nuclear Science and Technology Organisation, Menai, Australia. *Correspondence e-mail: chantler@unimelb.edu.au

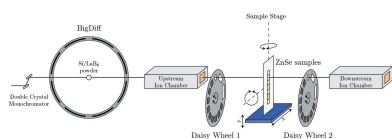
Measurements of mass attenuation coefficients and X-ray absorption fine structure (XAFS) of zinc selenide (ZnSe) are reported to accuracies typically better than 0.13%. The high accuracy of the results presented here is due to our successful implementation of the X-ray extended range technique, a relatively new methodology, which can be set up on most synchrotron X-ray beamlines. 561 attenuation coefficients were recorded in the energy range 6.8–15 keV with measurements concentrated at the zinc and selenium pre-edge, near-edge and fine-structure absorption edge regions. This accuracy yielded detailed nanostructural analysis of room-temperature ZnSe with full uncertainty propagation. Bond lengths, accurate to 0.003 Å to 0.009 Å, or 0.1% to 0.3%, are plausible and physical. Small variation from a crystalline structure suggests local dynamic motion beyond that of a standard crystal lattice, noting that XAFS is sensitive to dynamic correlated motion. The results obtained in this work are the most accurate to date with comparisons with theoretically determined values of the attenuation showing discrepancies from literature theory of up to 4%, motivating further investigation into the origin of such discrepancies.

1. Introduction

X-rays can act as direct probes into many systems, due to their strong depth penetration, energy-dependence and their non-destructive nature. Absorption and scattering interactions of X-rays are quantifiable, with the accuracy of measurements being dominated by the availability of accurate values for X-ray mass attenuation coefficients. In situations where attenuation coefficients are available and accurate, the absorption and scattering interactions of X-rays with matter can be used to create a more precise probe. X-ray absorption fine structure (XAFS) can measure dilute or disordered systems (Chantler *et al.*, 2015) which cannot be probed by other methods such as X-ray diffraction (XRD) or electron microscopy. This has led to new and important discoveries in a variety of disciplines from chemistry to biomedicine to agriculture (Waychunas *et al.*, 1993; Neidig *et al.*, 2011; Chevallier *et al.*, 2014).

XAFS consists of complex oscillations in the region above the edge of the X-ray absorption spectrum. Photoelectrons backscatter from neighbouring atoms toward the photoemitter causing quantum mechanical self-interference of the photoelectron with its own wavefunction.

Synchrotrons provide high-flux, dependable, coherent, tunable sources of X-rays. The first synchrotron revealed the potential of high-brightness X-ray sources (Johnston &



Tomboulou, 1954). Later, large-scale synchrotrons with storage rings were being designed and built (Kincaid & Eisenberger, 1975). The subsequent observation that XAFS is highly sensitive to small changes in local structure developed a field of probing regions close to a photoemitter. This sensitivity led to successful XAFS investigations of atomic structure, electron density, coordination number and the conformational properties of condensed matter systems (Stern, 1974; Rehr & Albers, 2000; Beale & Weckhuysen, 2010). XAFS is currently used to fingerprint materials in the X-ray absorption near-edge structure (XANES) region and to support structural conclusions about the dynamic local environment of (for example) partially disordered systems (Mathey *et al.*, 1985). XAFS analysis has precision enough to discriminate between alternate hypotheses for local bonding and nanostructure (Chandesris *et al.*, 1990).

The highly sensitive nature of XAFS has exposed long-standing discrepancies between theoretical calculations and experimental measurements of mass attenuation and has prompted improvement of its own measurement and analytical techniques. Improvements range from the introduction of curved wavefront corrections in the 1980s (Barton & Shirley, 1985a), the analysis of systematic and statistical errors in the 1990s (Filipponi, 1995; Booth & Hu, 2009), to more contemporary approaches using applications of density functional theory (Ladeira *et al.*, 2001; Bourke & Chantler, 2012). These improvements range from the development of high-pressure sample cells (Brugger *et al.*, 2007), to extended-range measurement techniques for high-accuracy quantification, and elimination of systematic errors (Tran *et al.*, 2003a; Chantler, 2009).

Several latest improvements are characterized by the X-ray extended range technique (XERT), where measurements are capable of determining mass attenuation coefficients with uncertainties below 0.1% for a several keV energy range. XERT has produced some of the highest-accuracy absolute-measurements of mass attenuation coefficients to date (de Jonge *et al.*, 2005). The accuracy is achieved by painstaking measurements during XERT experiments where, for example, all contributions to beam intensity are measured and all systematic effects precisely quantified, allowing corrections for these in subsequent analysis.

Modern X-ray physics is currently limited by the accuracy of attenuation coefficients. Despite X-ray attenuation being known and measured for over a century, claimed accuracies of mass attenuation coefficients are seldom better than 1–2%. This limits rigorous testing of atomic theories and renders deeper investigations unreliable (Chantler *et al.*, 1999, 2001). Medical diagnostics such as with computed tomography (CT) scans would yield better resolution given more accurate attenuation coefficients for the constitutional elements of the human body (Huang & Wu, 1976), with higher accuracy scans improving CT for example as a diagnostic tool.

In this work we use XERT to obtain the highest accuracy mass attenuation coefficients for zinc selenide. Zinc selenide is known to crystallize into two different atomic structures: zincblende (3C) and hexagonal close packed (2H/wurtzite)

(Huang & Ching, 1993; Triboulet *et al.*, 1995). The transition temperature of zinc selenide (Kikuma & Furukoshi, 1985; Fedorov *et al.*, 1991) from the 3C to 2H phase at standard pressure is over 1000°C (1425°C and 1680°C for the above references, respectively) with no regions where both structures can exist simultaneously. This is supported by numerous other X-ray diffraction (XRD) studies of the crystal structure which when conducted at room temperature have all found ZnSe to be in the zincblende phase (Indirajith *et al.*, 2014; Yang *et al.*, 2016; Kwon & Park, 2014). This work was conducted at 22°C so the zincblende structure is expected with lattice constant $a = 5.6696 \text{ \AA}$ (Sritharan *et al.*, 1984).

Most investigations of zinc selenide are in relation to its semiconductor properties with particular interest in the positioning of dopants implanted within the lattice (Cooper *et al.*, 2015). XAFS analyses of zinc selenide and most structural determination have investigated the Fourier transform of the fine-structure function (Diop & Grisenti, 1995; Kwon & Park, 2014) where uncertainties are often not propagated or estimated (Cooper *et al.*, 2015). The use of modern computational modelling with full propagation of experimental errors (Schalken & Chantler, 2018) allows for a more robust analysis than previously obtainable.

There has been a continued long-term inconsistency in the dispersion of X-rays leading to a breakdown of Friedel's law (Mair *et al.*, 1971) especially in the Bijvoet ratios of X-ray crystallographic structures of binary compounds with dual edges (Stevenson & Barnea, 1983a). Highly accurate mass attenuation measurements of zinc selenide are critical to address this.

XRD measurements of extended-face crystals including of zinc selenide (Stevenson & Barnea, 1983b; McIntyre *et al.*, 1980) show significant discrepancies between predicted theory for the Bijvoet ratios (B) given by

$$B = \frac{(I_H - I_{\bar{H}})}{(1/2)(I_H + I_{\bar{H}})}, \quad (1)$$

where I_H and $I_{\bar{H}}$ are the diffracted intensities from reflections of the form $\{h\bar{k}l\}$. Bijvoet Ratios can provide great insight into the determination of phases in structural analysis, in theoretically computed scattering factors and absolute configurations of molecules (Freeman *et al.*, 1977). Determination of the Bijvoet ratio usually proceeds by considering the transmission factor,

$$A = \frac{1}{2\mu} [1 - c \cos(\delta)], \quad (2)$$

where μ is the linear absorption coefficient, δ is the azimuth of the projection of the normal to the crystal surface in a plane parallel to the diffracting planes, and c is a constant. After correction for transmission, the ratios are strongly energy-dependent, and in particular the discrepancies with current extinction theory reach up to 6.4% for the 331 reflection which is far greater than the largest error estimates. This discrepancy has persisted for decades and there is still no theoretical prediction which matches the experimental results. Given the sensitivity of the Bijvoet ratios to thermal parameters, and to

both the imaginary and real component of the atomic form factor, an in-depth study of the X-ray absorption characteristics of zinc selenide should aid in promising a deeper understanding of this longstanding problem. It seems that the energy dependence of the ratios may be a critical and sensitive probe of anomalous scattering and perhaps of XAS.

2. Experimental details

Measurements were taken at the Australian National Beamline Facility (ANBF) using the bending magnet 20BM at the Photon Factory in Japan. After a Si (111) double-crystal monochromator and collimation to a 2 mm × 1 mm cross-sectional area, the X-ray beam was then passed through the high-resolution powder diffractometer BigDiff (Barnea *et al.*, 1992) utilizing powder diffraction samples in capillaries: National Institute of Standards and Technology (NIST) Standard Reference Materials (SRM) Si 640c and LaB₆ 660a. The incident and transmitted intensities through the samples were then recorded by two 18.5 cm ion chambers with the ionizing nitrogen gas flowed in series (see Fig. 1) in order to ensure high positive correlation between measurements (Chantler *et al.*, 2000).

To quantify the attenuation-dependent systematic errors such as detector linearity and harmonic content, three high-purity zinc selenide foils were chosen for this experiment, each having a cross-sectional area of 1 cm × 1 cm, with nominal thicknesses of 25 μm, 50 μm and 100 μm. These foil thicknesses were chosen such that at least one of them at a given energy would satisfy Nordfors' criterion [$2 < \ln(I_d/I_u) < 4$] (Nordfors, 1960), optimizing the signal-to-noise ratio of measurements. The foils were sourced from Crystran and synthesized from zinc vapour and H₂Se gas, forming sheets on graphite susceptors.

Directly upstream and downstream of the foils were two daisy wheels with apertures of varying sizes to quantify the scattered and fluorescent secondary photons produced by the sample. The daisy wheels also contained several aluminium foils of varying thicknesses used to measure the harmonic content of the beam.

3. Measurement and analysis

3.1. Measuring attenuation from count rates

Measurements of the incident and transmitted intensities of the X-ray beam were made by recording the number of counts in the respective ion chambers (Chantler *et al.*, 2000; Tran *et al.*, 2003a). The ion chambers produce a non-zero count rate when not exposed to any X-rays, the dark current, caused by both the leakage current and the electronic bias potential in the detection system. The effects of dark current become very important for thick foils at high attenuation (such as the immediate post-edge region where the XAFS is located) and can easily become a dominant source of uncertainty if not regularly monitored during the experiment. Each measurement was repeated ten times, in multiple combinations, so that measurements taken with the synchrotron beam off quantify the dark current, and average of the intensity ratios becomes

$$R = \frac{\overline{I_d - dc_d}}{\overline{I_u - dc_u}}, \quad (3)$$

where I_u is the upstream and I_d is the downstream ion chamber reading, and dc_u and dc_d are the upstream and downstream ion chamber dark current readings, respectively.

The ratio of the measured incident and attenuated intensities will also not be fully representative of the true attenuation of the sample due to the difference in the electronic amplification of the ion chambers, and the (air) absorption between the ion chambers.

To account for this effect ion chamber readings were recorded with no sample in the beam path – these are referred to as blank measurements. Once the blank measurements have been taken, we can relate the ion chamber readings to the mass attenuation coefficient via the Beer–Lambert law (Beer, 1852; Swinehart, 1962; Fuwa & Valle, 1963),

$$\left[\frac{\mu}{\rho}\right][\rho t] = -\ln \left[\frac{\left(\overline{I_d - dc_d}\right)_s}{\left(\overline{I_d - dc_d}\right)_b} \right], \quad (4)$$

where $[\mu/\rho]$ is the mass attenuation coefficient and $[\rho t]$ is the integrated column density, while the subscripts s and b refer to sample and blank signals, respectively. The measured

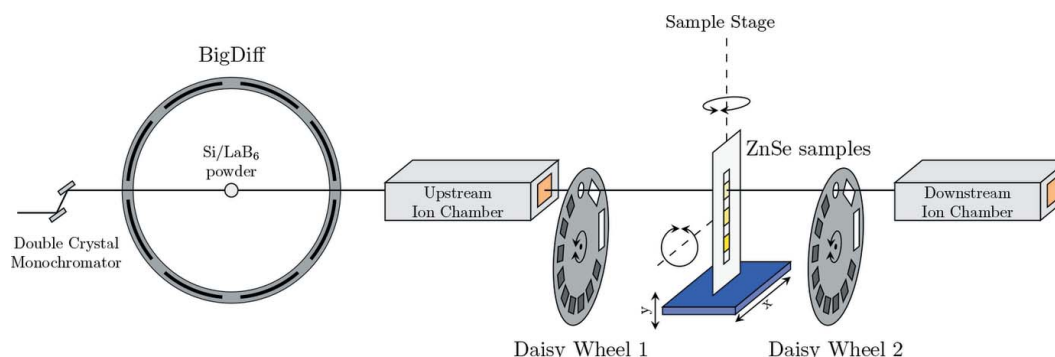


Figure 1

Schematic of the experimental layout. The collimated monochromatic beam was analysed in the BigDiff powder diffractometer to determine the beam energy. Ion chambers provided the monitor and detector signals for the experiment. Daisy wheels were configured to measure scattering and harmonic contributions. The three zinc selenide foils were mounted on the sample stage to determine the thickness-independent mass attenuation coefficient.

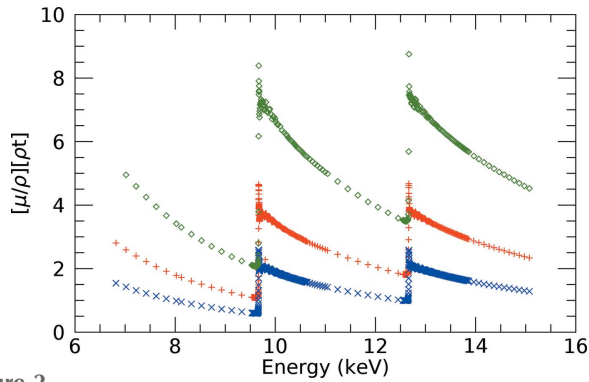


Figure 2
Measured attenuation $[\mu/\rho][\rho t]$ for 25 μm (\times), 50 μm ($+$) and 100 μm (\diamond). The attenuation level $[\mu/\rho][\rho t]$ varied from ~ 0.5 and ~ 8 , covering an approximately four orders of magnitude change in the attenuate intensity. Measuring this extended range of attenuation required precision calibration of the detection system and allowed accurate quantification of attenuation-dependent systematic errors.

attenuation of the three samples after correction for dark current and blank signals are displayed in Fig. 2.

The uncertainty in the repeated measurements for the intensity ratios is reported here as the standard error, which is added in quadrature with the uncertainty in the dark current measurements. These uncertainties become dominant for highly attenuating samples (Chantler *et al.*, 2012),

$$\sigma_R^2 = \sigma_{s.d.}^2 + \left[\frac{\partial I}{\partial (dc_d)} \Delta_{dc_d} \right]^2 + \left[\frac{\partial I}{\partial (dc_u)} \Delta_{dc_u} \right]^2 \quad (5)$$

$$= \sigma_{s.d.}^2 + \left[\left(\frac{I_d - dc_d}{I_u - dc_u} \right) \left(\frac{\Delta_{dc_u}}{I_u - dc_u} \right) \right]^2 + \left[\frac{\Delta_{dc_d}}{I_u - dc_u} \right]^2, \quad (6)$$

where $\sigma_{s.d.}$ is the standard deviation of the ratio of intensities (I_u/I_d). The final uncertainty in the attenuation of each foil is given by the quadrature sum of the blank measurement and the sample measurement,

$$\sigma_{[\mu/\rho][\rho t]} = \left[\left(\frac{\sigma_I}{I} \right)_s^2 + \left(\frac{\sigma_I}{I} \right)_b^2 \right]^{1/2}. \quad (7)$$

The blank and dark current are the two most critical corrections that must be made to any X-ray absorption data. In this work the dark current correction alone adjusted the final $[\mu/\rho]$ value of the 25 μm sample by up to 3.28%, while the 100 μm sample was corrected by up to 40.7%. The blank correction has an even more profound effect reducing the value of the mass attenuation coefficient for the 25 μm sample by up to 51.3% and the 100 μm sample by 23.1%. Although the magnitude of these corrections are very significant in most beamlines, and also herein, the very high count rates in both the upstream and downstream ion chambers mean that the blank normal-

ization introduces very little uncertainty into the resulting measurements.

3.2. Full-foil mapping procedure

The relative variation in the integrated column density of the 100 μm foil sample was mapped by scanning the beam across its total surface in step sizes smaller than the beam size of 2 mm \times 1 mm at 9.592 keV, an energy chosen as it lies just below the zinc *K*-edge, where the sample has low attenuation, making our readings less sensitive to systematic effects such as dark current errors and fluorescent scattering (see Section 5.2). This enables determination of the integrated column density of the central point of the foil through which the main attenuation measurements were carried out (de Jonge *et al.*, 2004a). The relative 2D map of the integrated column density is illustrated in Fig. 3 and indicates key structural features such as the perspex holder on the left and right on which the samples were mounted. The side edges were excluded for further analysis, as opposed to some other investigations using XERT. The significance of this on analysis is small but contributes to the absolute measurement uncertainty.

The average attenuation of the foil $\left[\overline{[\mu/\rho][\rho t]_{xy}} \right]_F$ can be directly related to the average integrated column density such that

$$\left(\overline{[\mu/\rho][\rho t]_{xy}} \right)_F = \left[\frac{\mu}{\rho} \right] \overline{[\rho t]_{xy}} = \left[\frac{\mu}{\rho} \right] \frac{m}{A}, \quad (8)$$

allowing for the absolute value of the mass attenuation coefficient to be determined with accurate knowledge of the mass m and the area A . The mass was measured using a microgram Mettler microbalance and the area was determined by mapping the perimeter of the sample with a series of points using an optical comparator and then using the formula

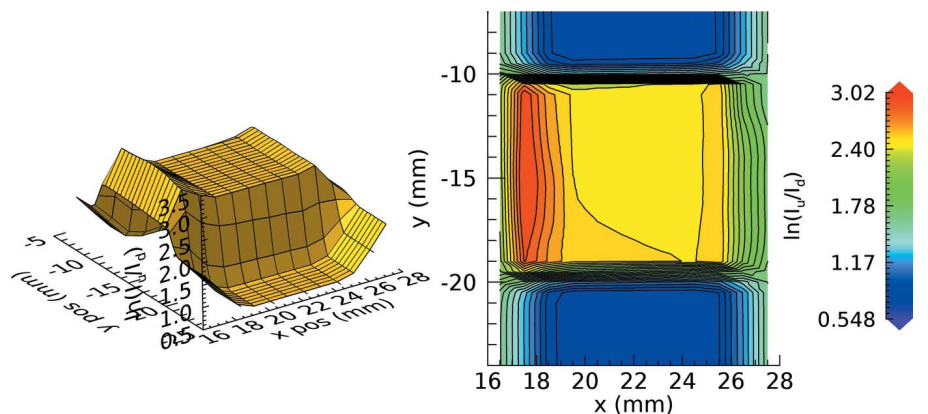


Figure 3
Attenuation profile of the 100 μm foil at 9.592 keV as a function of its x and y position and illustrating three regions of interest. The first is the near-flat central region where the beam only passes through the foil. The second region of interest is the sharp slopes at the top and bottom of the foil where only a fraction (a_x) of the beam is incident on the foil and the remainder passes through air. The third region relates to the two spikes to the left and right of the central region where the beam passes through both the foil and the perspex mount.

$$A = \frac{|\sum_{i=0}^{n-1} x_i y_{i+1} - \sum_{i=0}^{n-1} y_i x_{i+1}|}{2}, \quad (9)$$

where x , y are the horizontal and vertical coordinates of each point and n is the total number of points mapped.

The average foil attenuation was evaluated by

$$\overline{\left[\frac{\mu}{\rho}\right]_{\rho t}_{xy}}_F = \frac{\sum_i a_i \left(\left[\frac{\mu}{\rho}\right]_{\rho t}_i\right)}{\sum_i a_i}, \quad (10)$$

where a_i is the cross-sectional area of the beam hitting the foil, which is determined by examining and extrapolating the edge structure. The final uncertainty in the mass attenuation coefficient is

$$\frac{\Delta_{[\mu/\rho]}}{[\mu/\rho]} = \left[\left(\frac{\Delta_A}{A}\right)^2 + \left(\frac{\Delta_m}{m}\right)^2 + \left(\frac{\Delta_{[\mu/\rho][\rho t]}}{[\mu/\rho][\rho t]}\right)^2 \right]^{1/2}. \quad (11)$$

In order for equation (8) to be valid, the foils must be oriented perpendicular to the X-ray beam, yet the foils are always slightly misaligned by an angle θ . This misalignment leads to the effective thickness of the foil changing as $t/\cos(\theta)$ and hence should be quantified and corrected. This was done by fitting such a model to additional attenuation measurements taken of the foil as its orientation was varied in both the horizontal and vertical directions. This correction to the attenuation and its resulting uncertainty were both explicitly measured to be insignificant in comparison with other sources of error.

The average attenuation determined by the full-foil mapping procedure was $\overline{[\mu/\rho][\rho t]} = 1.93597$ with $\Delta_{[\mu/\rho][\rho t]} = 0.017\%$ leading to a mass attenuation value of $[\mu/\rho] = 40.0043 \pm 0.13\%$ ($\text{cm}^2 \text{g}^{-1}$) with the error being dominated by the uncertainties Δ_A and Δ_m . The thickness of the foil at the central position where the main measurements were taken was therefore determined to be $t = 90.9652 \mu\text{m} \pm 0.130\%$.

3.3. Uncertainty of full-foil mapping

After systematic corrections, the mass attenuation coefficient at each energy is then determined by taking the weighted average of all three foils $i = 1 \rightarrow 3$. The statistical uncertainty r from the variance of the absorption measurements is

$$(\Delta_{[\mu/\rho]})_r = \left[\frac{\sum_i w_i ([\mu/\rho]_i - \overline{[\mu/\rho]})^2}{N \sum_i w_i} \right]^{1/2}, \quad (12)$$

where $w_i = 1/\sigma_i^2$ and N is the total number of measurements. Hence the absolute uncertainty (a) is

$$\frac{(\Delta_{[\mu/\rho]})_a}{[\mu/\rho]} = \left\{ \left[\frac{(\Delta_{[\mu/\rho]})_r}{[\mu/\rho]} \right]^2 + \left[\frac{(\Delta_{[\mu/\rho]})_{ff}}{[\mu/\rho]_{ff}} \right]^2 \right\}^{1/2}, \quad (13)$$

where the subscript ff represents the full-foil mapping result of the previous section.

4. Determination of photon energies

The photon energies for this experiment were determined by recording powder diffraction patterns of NIST SRMs LaB₆ (660a) and Si (640c). All diffraction measurements were made using the BigDiff powder diffractometer set up in Debye–Scherrer geometry (Fig. 4). The image plates used to detect the diffracted X-rays are placed around the inside surface of a (large 100 cm radius) cylinder and the powder is placed in capillaries aligned with the beam axis along the centre of the cylinder. 2θ records the position of the diffraction peaks.

The specific image plates used in this experiment were photostimulable phosphor plates, five to eight of which were used in this experiment with each one recording a different angular range. Between exposures image plates were translated behind internal slits, producing a sequence of narrow strips containing diffraction patterns. Image plates were digitized by a Fuji BAS2000 scanner (Cookson, 1998). Images of radioactive fiducial markers inset at known positions at the edges of the BigDiff image plate holders appeared on each image plate. These were used to assign the angular scale for the diffraction patterns as part of the image plate data extraction process using *PPDA* (Hester *et al.*, 2020). This data was then used to obtain a directly analysable intensity versus angle diffraction spectrum where it is then possible to determine the exact centre of each of the diffraction peaks by fitting a Voigt spectral profile with a quadratic background to each one and extracting the centroid value. Each peak was then assigned an *hkl* Miller index in a highly automated process.

Once each peak had been assigned the correct *hkl* value it could be simultaneously fitted to the modified form of the Bragg equation,

$$\sin(\theta + \delta\theta_{p_i} + \delta\theta_y + \delta\theta_z) = \frac{hc}{2dE_{\text{cal}}}, \quad (14)$$

with

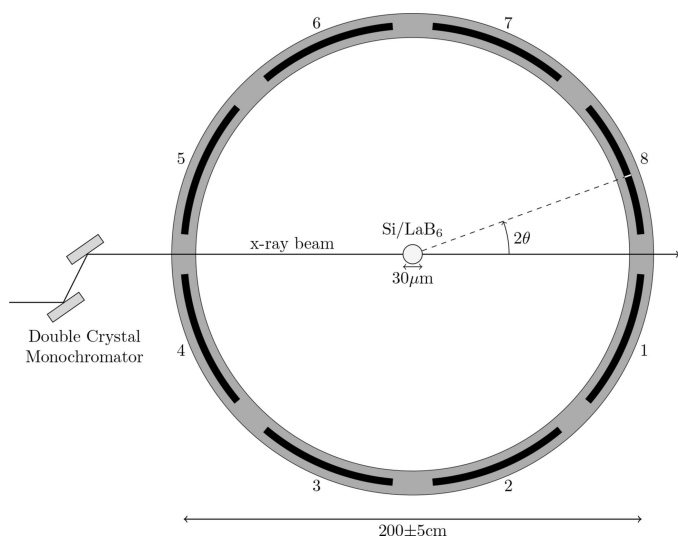


Figure 4 Schematic of the BigDiff powder diffractometer. Numbers ranging from 1 to 8 label the image plates that were collected and analysed.

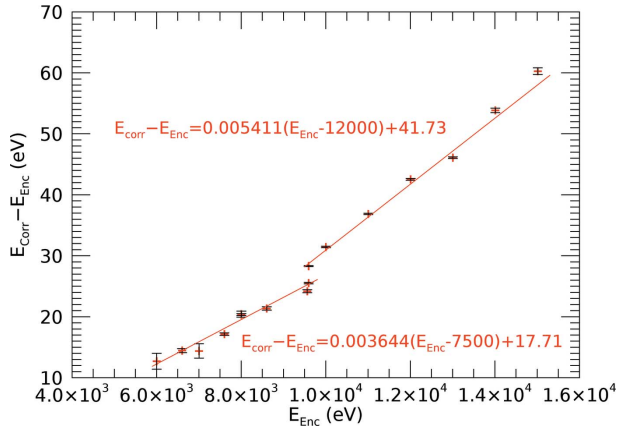


Figure 5
Calibration curve of measured energies versus the nominal encoder energies fitted to determine the correction to nominal encoder energies.

$$\delta\theta_y = \frac{\delta_y}{R} \cos(2\theta) \quad \text{and} \quad \delta\theta_z = \frac{\delta_z}{R} \cos(2\theta), \quad (15)$$

where δ_y and δ_z are the small vertical and horizontal sample offsets in alignment of the beam from the centre of BigDiff, R is the distance from the capillary to the image plates, θ_{p_i} is the image plate offset for the i th plate and d is the lattice spacing.

Each energy was fitted separately with all plates fitted simultaneously. The goodness of fit χ_r^2 never exceeded 4.6, indicating that our model was accurate. Two independent linear fits modelled the data (Fig. 5),

$$E_{\text{corr}} - E_{\text{Enc}} = c + m(E_{\text{Enc}} - E_0), \quad (16)$$

where E_{corr} is the corrected energy, E_{Enc} is the encoder energy from the monochromator, and E_0 is a reference energy in the middle of the data in order to reduce correlations in our final uncertainties. Above 9.5 keV, where the harmonic content was insignificant, the monochromator was tuned to maximize the incident intensity. Below 9.5 keV, where the harmonic content can become increasingly significant, the monochromator was detuned to minimize the harmonic content, which naturally changes the beam energy compared with a nominal encoder calibration.

The fit resulted in the following values: $c_1 = 17.71 \pm 0.12$ eV, $m_1 = 3.644 \times 10^{-3} \pm 7.8 \times 10^{-5}$ and $c_2 = 41.73 \pm 0.06$ eV, $m_2 = 5.411 \times 10^{-3} \pm 3.6 \times 10^{-5}$ for the first and second linear regions, respectively.

The corresponding uncertainty is calculated using the covariance matrix. The uncertainty, defined as the root mean square of the residuals, is

$$\sigma = \frac{\sum_j [(E_{\text{corr}} - E_{\text{Enc}})_j - E_{\text{fit}_j}]^2}{\sigma_j^2} \bigg/ \sum_j \frac{1}{\sigma_j^2}, \quad (17)$$

where $(E_{\text{corr}} - E_{\text{Enc}}) - E_{\text{fit}}$ are the residuals of the fit shown in Fig. 5. Evaluation of this gives an additional 0.93 eV to the uncertainty of the first fit and 0.82 eV to the second.

5. Correcting for systematic errors

5.1. Harmonic contamination

Determination of the harmonic component of the synchrotron beam followed Tran *et al.* (2003b). The process involves measuring the attenuation of 15 aluminium foils that ranges from 10 to 4000 μm and measurements were taken every 1–2 keV from 15 keV down to 8 keV. These attenuation measurements are then fitted to the following equation,

$$\frac{I}{I_0} = (1 - H_{\text{eff}}) \exp\left\{-\left(\left[\frac{\mu}{\rho}\right]_f [\rho t]\right)\right\} + H_{\text{eff}} \exp\left\{-\left(\left[\frac{\mu}{\rho}\right]_h [\rho t]\right)\right\}, \quad (18)$$

where H_{eff} is the effective harmonic parameter and $[\mu/\rho]_f$ and $[\mu/\rho]_h$ are the attenuation coefficients at the fundamental and higher-order harmonic energies.

Because of ideal detuning, harmonic content was insignificant and below measurement uncertainty. This method has been used successfully at the 20B beamline of the Photon Factory to determine harmonic content of the beam (Glover *et al.*, 2008). Previous studies have detected harmonics below 8 keV but it has been found negligible at higher energies.

5.2. Fluorescence

Secondary photons in the form of X-ray fluorescence can cause a systematic error in the measured mass attenuation coefficient (Tran *et al.*, 2004) and were clearly observed in this data. Fluorescence is most prominent in energy regions just above the zinc and selenium K -edges, where the emitted K_α and K_β photons enter the detectors causing the systematic error.

Fluorescence was most prominent for thicker samples having up to a 0.4% effect on our final measurements. Fluorescent emission is isotropic, so varying the aperture size allows us to measure the fluorescence magnitude (Glover *et al.*, 2010). Here we must model contributions from both the zinc and selenium K -edges simultaneously. The effect was modelled by interpolating the K -edge absorption tables generated by NIST (Chantler, 1995) for both zinc and selenium.

These values were combined to obtain values of the K -edge absorption of zinc selenide by using

$$\left[\frac{\mu}{\rho}\right]_{\text{ZnSe}} = w_{\text{Zn}} \left[\frac{\mu}{\rho}\right]_{\text{Zn}} + w_{\text{Se}} \left[\frac{\mu}{\rho}\right]_{\text{Se}}, \quad (19)$$

where w_{Zn} and w_{Se} are the fractions by atomic weight of zinc and selenium in zinc selenide, respectively.

After correction, we see good agreement in attenuation across all apertures and energies. The resultant contribution to uncertainty was given by examining the difference in the average value of the downstream count rates between the smallest and largest apertures. This error in the count rate is then added to Δc_d in equation (6). The estimated uncertainty is a slight overestimate, as the smallest aperture result will always be close to the true value of $[\mu/\rho]$ and any deviation

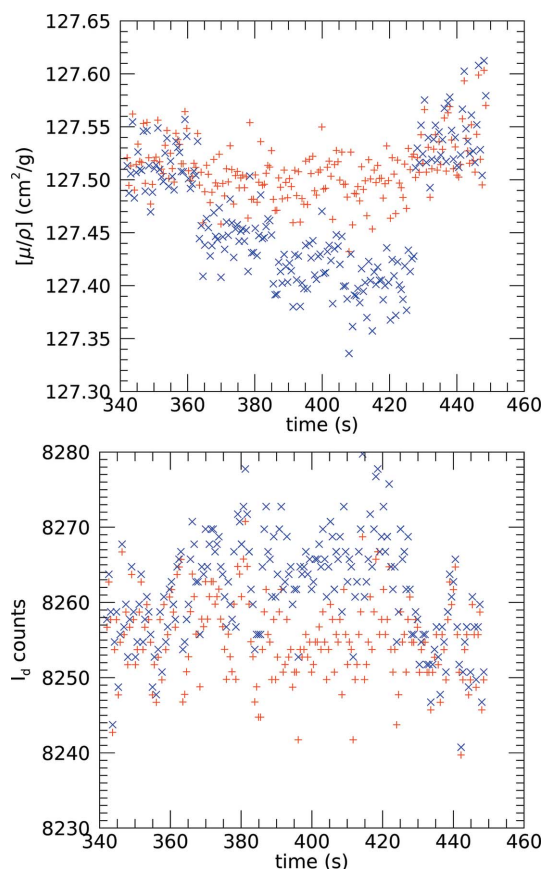


Figure 6
Effect of our correction for fluorescent scattering showing uncorrected (×) and corrected (+) measurements, showing both the attenuation data (top) and downstream ion chamber readings (bottom). With all 200 readings repeated at the same energy the data is broken up into five segments, each containing 40 one-second measurements, where different daisy wheel apertures were being used. Both the attenuation and count rates are far more consistent across the apertures after correction, with the value of $[\mu/\rho]$ increasing by 0.056% and the associated uncertainty reducing from 5.743×10^{-3} to 2.255×10^{-3} . The additional error in the count rates was determined to be 2.9 counts, which was reduced from 9.0 counts prior to the correction. Ultimately the total relative error in $[\mu/\rho]$ decreased from 7.25×10^{-3} to 2.92×10^{-3} as a result of this, even when factoring in the additional error for the count rate. The effect of fluorescence on upstream ion chamber readings is negligible due to their high count rates.

from this will come from an over- or under-correction for the larger apertures. The magnitude of the correction due to fluorescence to the value of $[\mu/\rho]$ is small with the maximum correction to the 25 μm , 50 μm and 100 μm samples being 0.046%, 0.11% and 0.67%, respectively. The correction is largest within the XAFS region and varies with attenuation, so can significantly alter the fine structure even after background subtraction. This makes this correction important (Fig. 6).

We investigated the possibility of ionization of the zinc atoms by the (selenium) fluorescent photons absorbed by zinc atoms, emitting additional fluorescent photons that reach the detectors, because the energy of the selenium K_α and K_β photons are above the K -edge of zinc. A model was constructed and the effect was found to have negligible contributions across all foils, apertures and energies.

5.3. Monochromator drift

Monochromator drift is seen regularly in data from several beamlines and certainly from ANBF. After a (large) change of energy to the next step, the monochromator gearing takes some time to settle so that the true energy of the beam is drifting with time even while the feedback monochromator encoder might have settled, and indeed this process can take a couple of minutes. It is better to characterize this with step measurements and continuous scan measurements will have this with an unknown and uncalibratable magnitude.

In our method, the first 20 s after a change in energy were spent taking dark current measurements, allowing the monochromator to settle by the time most attenuation measurements started. The experiment was constructed with either the 25 μm or 100 μm sample recorded first, so that the 50 μm sample was always completely unaffected by this systematic and can monitor the systematic. The effects of monochromator drift were observed in a handful of measurements in this experiment, when the stepwise change in energy and monochromator angle was large, greater than 50 eV, so the XAFS region was unaffected.

The energy drift ΔE_{drift} is dependent upon the step size in energy ΔE as well as the time since the change in energy Δt ,

$$\Delta E_{\text{drift}} = \alpha \Delta E \exp\left(\frac{-\Delta t}{\tau}\right). \quad (20)$$

α and τ were fitted parameters. The resultant change in the measured mass attenuation coefficient is then given by

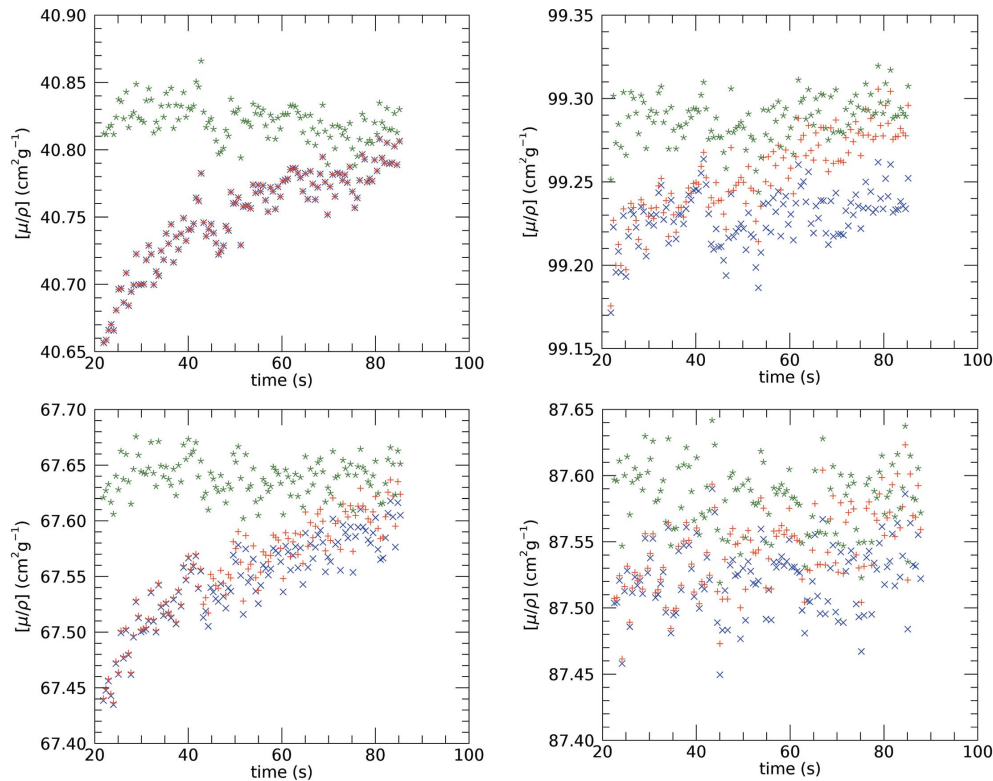
$$\Delta_{[\mu/\rho]} = \Delta E_{\text{drift}} \frac{d[\mu/\rho]}{dE}. \quad (21)$$

The time constant τ of 33.6 ± 1.8 s shows good agreement with previous work at this beamline (Glover *et al.*, 2008). The magnitude of the drift at time $t = 0$ [α in equation (20)] was found to be 0.106 ± 0.04 eV. The model was used to correct for the effect of monochromator drift on the affected measurements and the appropriate uncertainty contributions were included (Fig. 7).

The error introduced by the correction was taken to be the difference in the resulting correction when adjusting τ and α by the error of their respective fits. The maximum correction was found to be 0.159% at 9.3298 keV with the resulting uncertainty being 0.0167%. This systematic was small (Glover *et al.*, 2008) and only became noticeable after correction for the fluorescent contributions. Whilst not a dominant systematic herein, monochromator drift is important to keep track of, especially when taking fewer more widely spaced attenuation measurements where the corrections can become more significant, or when calibrating other continuous scan measurements.

5.4. Bandwidth

The bandwidth of the beam depends upon the finite distribution of the lattice spacing of the monochromator under thermal stress, the acceptance angle and the divergence of the


Figure 7

Results indicating the presence and correction of monochromator drift showing the raw data (\times), the data that has had fluorescent scattering applied ($+$) and the final drift corrected data (\star). These examples show 120 repeated one-second measurements taken for the 25 μm sample. These measurements were collected at 9.330 keV (below the edge, top left), 10.639 keV (top right), 12.252 keV (bottom left) and 14.670 keV (bottom right). Note that at 9.330 keV raw and fluorescence corrected data are identical as are below the zinc K -edge. At 10.639 keV and 12.252 keV, the effect of drift only becomes evident after correction for fluorescence.

incident beam (de Jonge *et al.*, 2004b). The Beer–Lambert law must be rewritten as

$$\exp\left(-\left[\frac{\mu}{\rho}\right][\rho t]\right) = \frac{\int_0^\infty I_d(E) dE}{\int_0^\infty I_u(E) dE}, \quad (22)$$

where $I_u(E)$ represents the intensity of the incident beam at the upstream detector and $I_d(E)$ represents the intensity of the beam at the downstream detector, at each energy E in the bandwidth. If we assume that the incident intensity profile is a Gaussian, then the correction from the ideal mass attenuation measurement in terms of r_w , the range over which we are sampling the Gaussian distribution, and s_{FW} , the sampling frequency, becomes

$$\Delta E_{\text{bandwidth}} = \frac{1}{\rho t} \ln \left[\sum_{k=-j}^j \tilde{I}_u(E_0 + k\Delta E) \times \exp\left\{-\frac{d[\mu/\rho]}{dE}(k\Delta E)\right\} \right], \quad (23)$$

where $j = r_w(s_{FW} - 1)/2$, $\Delta E = \text{FWHM}/(s_{FW} - 1)$ and $\tilde{I}_u = I_u / \int_0^\infty I_u dE$ is the normalized incident mean energy profile. The gradient $d[\mu/\rho]/dE$ was evaluated by taking the numerical derivative of the weighted mean of the 25 and 50 μm samples using the three-point Lagrangian interpolation method of Hildebrand (1987). s_{FW} is an odd integer.

The FWHM of the Gaussian profile was found to be 3.09 ± 0.08 eV and 5.80 ± 0.080 eV at the zinc and selenium K -edges, respectively. These are much larger than were measured at 20 keV for this beamline with different conditions and detuning (de Jonge *et al.*, 2004b). Hence this correction is much more significant over a couple of widths across and above the absorption edges. However, compared with Tantau *et al.* (2015) at 25 keV, again at the same beamline, the correction is significantly lower. These are real observed variations due to the monochromation and collimation of the X-ray beam under different experimental conditions, even at the same beamline. These values were then used to apply correction to the attenuation (Fig. 8) where we see significant reduction in the systematic effect of bandwidth. As with monochromator drift, the error introduced by the correction was taken to be the difference in the resulting correction when adjusting the FWHM by the error of the fit.

Whilst the effect of bandwidth only affects a small number of near-edge measurements, leaving the extended fine-structure region mostly untouched, its correction can have a very pronounced effect on edge and pre-edge structure, and on the definition of the edge or E_0 . In this work we observed a shift in $[\mu/\rho]$ of the 50 μm sample by 18.6% and the 25 μm sample by 10.2% and introduced uncertainties of 1.07% and 0.59%, respectively. Hence the final weighted correction is a maximum of 11.9% with the maximum uncertainty of 1.2% at

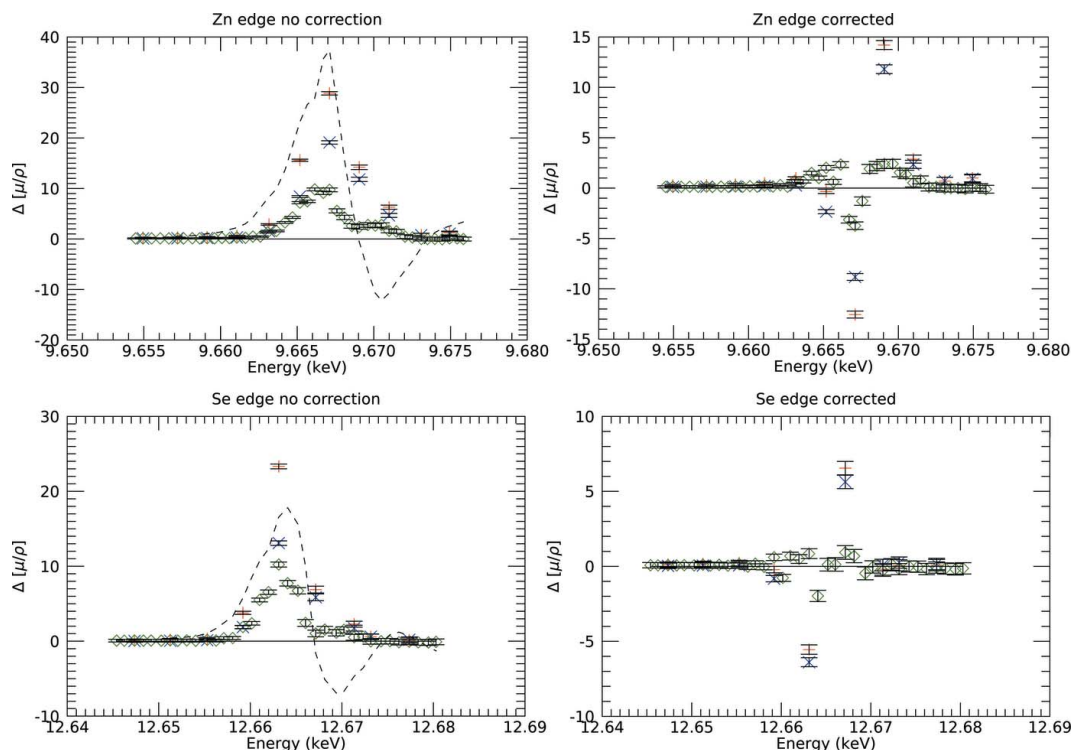


Figure 8 (Left) The finite bandwidth of the incident beam is indicated by the deviations from 0 of the difference between measurements using different foil thicknesses, correlated with the gradient of the mass attenuation coefficient. (Right) Effects of the applied correction for 25–50 μm (◇), 50–100 μm (×) and 25–100 μm (+). The dashed line represents a plot of a percentage of $d[\mu/\rho]/dE$ on a relative scale.

the same energies. This is orders of magnitude larger than either fluorescent or monochromator drift. Systematic measurement and correction of bandwidth is extremely useful in characterizing the near-edge structure (XANES). XANES is a powerful analytical tool (Babonneau *et al.*, 1988; Rehr & Ankudinov, 2005).

6. Final results and error analysis

Plots of the XAFS regions can be seen in Fig. 9. The energy spacing decreases further away from each absorption edge. The energy spacing remains finer for longer above the selenium edge, which should allow for more accurate structural analysis compared with the zinc edge.

6.1. Comparison of edge energies

Following Kraft *et al.* (1996), we may define the operational experimental edge energy as the lowest energy inflection point. Then our measured absorption *K*-edge energies are 9.6667 (12) keV and 12.6631 (13) keV for zinc and selenium, respectively. This is approximately 6 eV and 5.3 eV higher, respectively, than those reported by Kraft *et al.* (1996) for zinc metal [9.66047 (8) keV] and pure selenium reported by Bearden & Burr (1967) [12.6578 (7) keV]. The values of Bearden & Burr (1967) are themselves slightly inconsistent from the higher accuracy reports of Kraft *et al.* (1996), tending to be slightly lower overall. We expect to see chemical shifts (Sarode *et al.*, 1979) of the absorption edges for compounds

towards the higher end of the energy spectrum. Previous studies on zinc selenide found that both the zinc and selenium edges can shift by around +2 eV with some significant uncertainty (Vishnoi & Agarwal, 1969; Iwanowski *et al.*, 1997). Data from experiments that are useful for our comparisons are currently available from an online database located at The University of Chicago (Newville, 2016), although we proceeded with some caution. With no quoted accuracy on the energy measurements provided, the extent of systematic

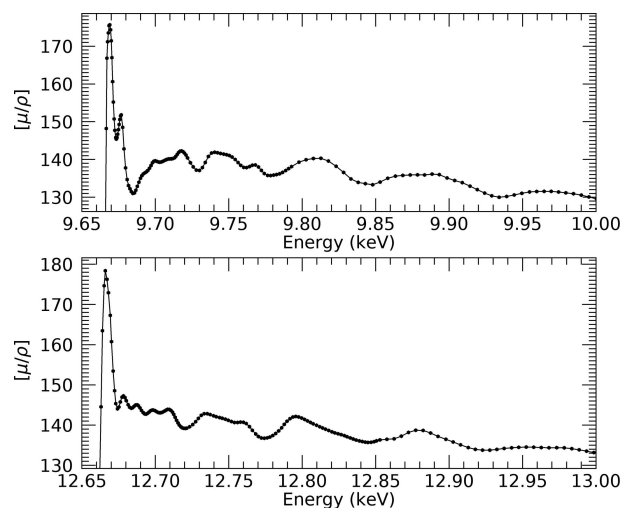


Figure 9 Corrected absolute mass attenuation coefficients and structure in the XAFS regions of the zinc (top) and selenium (bottom) *K*-edges.

corrections applied is unclear, and so the uncertainty and systematic corrections are not known (Newville, 2016). Whilst remaining mindful of our concerns, we can report that a similar analysis with this data returns values of 9.6638 (1) keV and 12.6578 (1) keV for the zinc and the selenium *K*-absorption edges, respectively. These results are 3.3 eV higher than those obtained by Kraft *et al.* (1996), and 3.2 eV lower than our result for selenium.

6.2. Determination of photoelectric attenuation

The two leading theoretical tabulations for mass attenuation coefficients, FFAST and XCOM, estimate elastic (coherent) scattering contributions in the form of Rayleigh scattering (*i.e.* isolated atom, incoherent scattering), into their calculations to estimate the total attenuation,

$$\left[\frac{\mu}{\rho}\right]_{\text{tot}} = \left[\frac{\mu}{\rho}\right]_{\text{PE}} + \left[\frac{\mu}{\rho}\right]_{\text{R}} + \left[\frac{\mu}{\rho}\right]_{\text{C}}, \quad (24)$$

where $[\mu/\rho]_{\text{PE}}$ is the attenuation due to photoelectric absorption and $[\mu/\rho]_{\text{R}}$, $[\mu/\rho]_{\text{C}}$ are the contributions due to Rayleigh and Compton scattering, respectively. Hence to remove the Compton scattering contribution from our measured results we read in the respective $[\mu/\rho]_{\text{C}}$ for zinc and selenium and combine them using equation (19). Inelastic, incoherent scattering contributions such as Compton scattering are known to not add linearly (Bourke & Chantler, 2014); and elastic scattering contributions (diffraction) are far from linear and are coherent. To account for this we estimate an uncertainty of 10% as this is likely to be an overestimate of the true error based on previous calculations and comparisons of Compton scattering (de Jonge *et al.*, 2005). However, while Rayleigh scattering is a good approximation in isotropic disordered materials such as pure zinc and selenium, ZnSe is a crystal where the interaction is highly coherent (Chantler & Barnea, 1999). For perfect crystals such as Si, Ge or even a moderate crystalline ZnSe, there are two alternative estimates of elastic scattering contributions. The first is due to constructive interference for any Bragg reflections from lattice planes of the crystal aligning with the X-ray beam at the requisite angles and energy. These processes are usually clearly visible when looking at the attenuation data and we do not observe any of these ‘Bragg glitches’.

The second alternative estimate for elastic scattering is that of thermal diffuse scattering (TDS), where the coherence is located at the extremum for destructive interference. This ensures a much lower value than anticipated for Rayleigh scattering by an order of magnitude or more. TDS arises from the dynamic, random thermal motion of the atoms within the crystal, breaking the crystal symmetry, which contributes to elastic scattering. The total attenuation for a crystal is then expressed as

$$\left[\frac{\mu}{\rho}\right]_{\text{tot}} = \left[\frac{\mu}{\rho}\right]_{\text{PE}} + \left[\frac{\mu}{\rho}\right]_{\text{TDS}} + \left[\frac{\mu}{\rho}\right]_{\text{C}}, \quad (25)$$

where $[\mu/\rho]_{\text{TDS}}$ is the attenuation due to thermal diffuse scattering (Gerward & Thuesen, 1977).

The thermal diffuse scattering cross section for the approximation of independent vibration of the atoms can be written as (Sano *et al.*, 1969)

$$\sigma_{\text{TDS}} = \frac{1}{2} r_e^2 \int_{-1}^1 [1 + \cos^2(\Phi)] |f(x, Z)|^2 \times \{1 - \exp[-2M(x, Z)]\} 2\pi d[\cos(\Phi)], \quad (26)$$

where r_e is the classical electron radius, $x = \sin(\Phi/2)/\lambda$, $f = f_0 + f' + if''$ is the complex atomic form factor and $\exp[-2M(x, Z)]$ is the Debye–Waller factor. f_0 is the atomic scattering factor and is a function of the scattering angle θ , the wavelength of the X-rays λ and the atomic number Z . Values for f_0 (Wilson & Geist, 1993) and f_1 and f_2 (Chantler, 2000) were converted using $f' = f_1 - f_{\text{rel}} - Z$ and $f'' = f_2$. The Debye–Waller factor is $\exp(-2Bx^2)$, with $B_{\text{Zn}} = 1.020 \text{ \AA}^2$ and $B_{\text{Se}} = 0.739 \text{ \AA}^2$ (McIntyre *et al.*, 1980). Given the dependence on the atomic form factor we calculate the values of the TDS cross section for zinc and selenium with their corresponding B and f values using equation (19). Similarly to Compton scattering we estimate an uncertainty of 10% based on comparisons between various different calculations of the TDS cross section (Tran *et al.*, 2003a); again this is likely an overestimate of the error.

This cross section can then be related back to the mass attenuation coefficient contribution,

$$\sigma_{\text{TDS}} = \frac{[\mu/\rho]_{\text{TDS}} m_a}{N_A}, \quad (27)$$

where m_a is the atomic molar mass and N_A is Avogadro’s number.

Since the elastic scattering is observed to follow a thermal diffuse scattering estimate from the data, this is quite a small contribution to remove. Inelastic scattering becomes dominant at higher energies but is quite modest across these edges.

The calculated additional attenuation contributions (Fig. 10) use Compton scattering obtained from (Berger & Hubbell, 1987) and interpolated. As expected, both contributions are

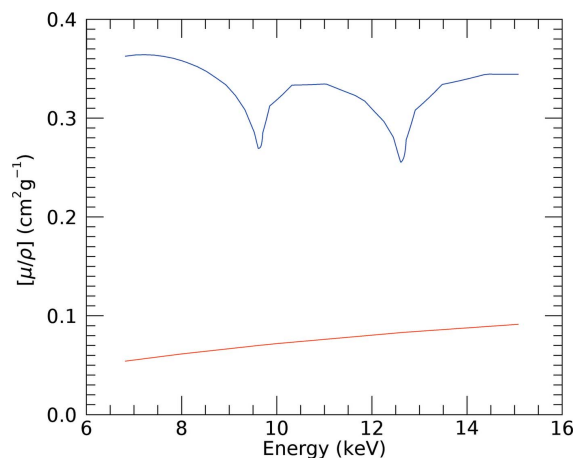


Figure 10 Attenuation of thermal diffuse scattering (blue) and Compton scattering (red) for zinc selenide across the measured energy range.

small relative to the total attenuation with the TDS correction having a maximum of 0.70% at 9.33 keV and a minimum of 0.15% at 12.67 keV. The Compton scattering contribution is even smaller with a maximum of 0.17% at 9.63 keV and a minimum of 0.040% at 9.67 keV.

6.3. Comparisons with theory

Fig. 11 shows comparisons between the measured results of the mass absorption (photoelectric) coefficient and the corresponding predicted theoretical values. Theoretical tabulations were interpolated and combined using equation (19) for each experimentally measured energy. The density of ZnSe is particularly uncertain. We may normalize either above the Zn or well above the Se edge, *i.e.* at either 12 keV or 15 keV at the top or bottom pair of plots of Fig. 11. Theoretical tabulations are at best accurate to about 1% (Chantler, 2000). Whilst the reference density of ZnSe is 5.27 g cm^{-3} at 22°C

(Wyckoff, 1963), with a linear expansion coefficient of $4.96 \times 10^{-6} \text{ K}^{-1}$ (Su *et al.*, 2009), we obtain a 1.9% and 3.8% correction of the density normalized at 12 keV, or a 2.9% and 4.2% correction normalized at 15 keV for the FFAST and XCOM tabulations, respectively. The difference between these two set points is significantly less than the uncertainty, and the overall normalization is also within expected uncertainty. Hence this does not yet distinguish clearly between these theoretical approaches nor between theory and experiment.

The FFAST database is the best predictor of the near-edge region at this time. XCOM has a much larger ‘triangle effect’ error in the near-edge region, and also a larger offset of the energy with respect to experiment. This is common for most elements thus far investigated (Tran *et al.*, 2003c, 2005; Glover *et al.*, 2010). Above the zinc *K*-edge, FFAST appears to have converged more uniformly. However, below the zinc *K*-edge, XCOM appears to have improved, with a discrepancy of $1\% \pm 1\%$ versus an estimated $3\% \pm 1\%$ for FFAST. Note, however, that the density was normalized an extra 2% for XCOM which might imply they are consistent in their approximation below the edge. The oscillation near the edges is a manifestation of the XAFS in the experimental data, compared with the theoretical free-atom approximation, which thus do not model the solid state photoelectron interference.

The discrepancy of FFAST at low energies below edges has been attributed (de Jonge *et al.*, 2005) to a limitation of convergence within the older relativistic wavefunction code of the time compared with non-relativistic codes. Whilst the relativistic forms are considered more accurate, they still include significant approximations. Indeed the non-relativistic codes are more stable for convergence of outer shell wavefunctions. On this basis, XCOM can sometimes be a preferred estimate for low energies.

Scofield (1973, 1974) and Perkins *et al.* (1991) have discussed and provided two theoretical predictions for atomic absorption coefficients – the unrenormalized values in XCOM and another renormalized set, obtained by renormalizing the cross sections by the amplitude of the potential at the nucleus, in a relativistic Hartree–Fock potential compared with XCOM’s Hartree–Slater potential. The decision as to whether or not to perform this renormalization has been an ongoing discussion in the field. Some previous investigations have favoured the unrenormalized results (Saloman & Hubbell, 1987; Gerward, 1992). Those comparisons were made with significantly less accurate experimental data than that presented in this work, making a definitive resolution to this discussion impossible. Comparisons between the two calculations are shown in Fig. 12, this time with no density normalization, where it is evident that performing these renormalizations does result in some slight improvement in the high-energy post *K*-edge regions. However, below the zinc edge and near the edges, significant deviations of the renormalized predictions are observed. The Hartree–Fock calculations are highly inconsistent in their agreement with the data in comparison with the Hartree–Slater ones. This current evidence continues to favour the less-fully relativistic unre-

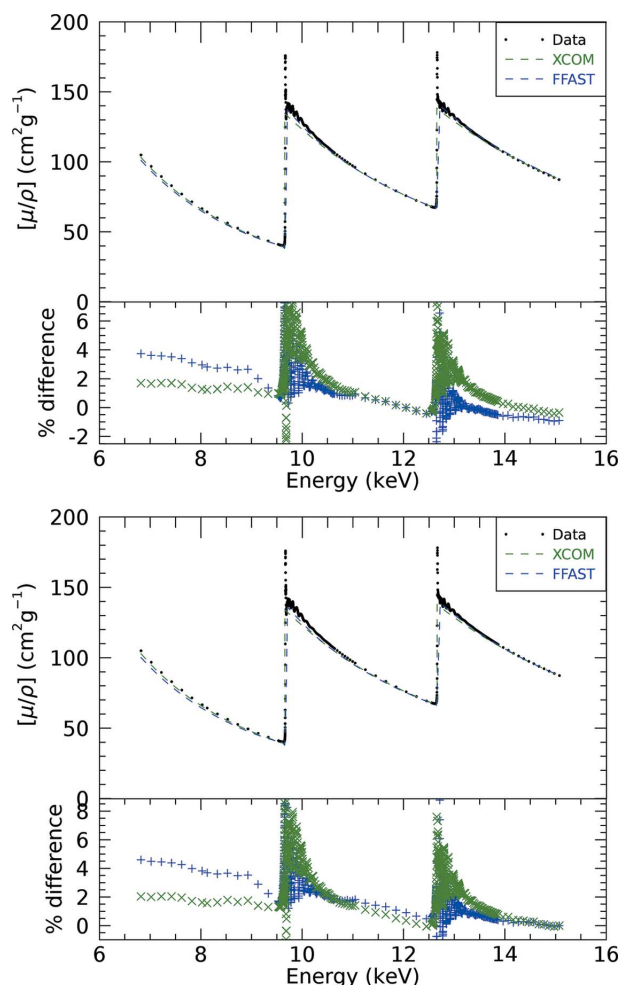


Figure 11 Comparison of the experimental mass absorption coefficient with two corresponding theoretical results. (Top panel) Density normalized at 12 keV. (Bottom panel) Density normalized at 15 keV. The upper graphs in each panel show the values of the mass attenuation coefficient as determined by this experiment and those predicted by FFAST (Chantler, 2000) and XCOM (Berger & Hubbell, 1987) tabulations. The lower graphs in each panel show the percentage discrepancies between the measured data [zero line], FFAST [+] and XCOM [×].

Table 1

Error analysis: magnitude of specific experimental systematics and their correction and uncertainties from these on final results; absolute accuracy of the full-foil mapping technique; error in the fit of the energy calibration HEADNT.

Quantity	Magnitude		Uncertainty ($\pm 1\sigma$)		Contribution†
	Near edge	Far edge	Near edge	Far edge	
$[\mu/\rho]_{\text{rel}}$	0.046% – 0.118% (50 μm) – 0.67% (100 μm) < 11.9% 0	0 < 0.15% Up to 3.3% (25 μm) – 40.7% (100 μm) 0.328% – 7.237%	< 0.01% < 1.2% 0	0 0 < 0.016% 0.00147% – 0.0185% $2.67 \times 10^{-5}\%$ – $4.82 \times 10^{-4}\%$ 0.00134% – 0.580%	Fluorescence #1 Bandwidth #2 Mono drift #3 Dark current #4 Variance #5 Relative uncertainty #6
$[\mu/\rho]_{\text{abs}}$		– 7.6% – 25% (100 μm) – 51% (25 μm)		0.129% $8.32 \times 10^{-6}\%$ – $3.6 \times 10^{-5}\%$	Full foil #7 Blank normalization #8
E		0.223% – 0.385%		0.00655% – 0.0163%	Energy #9

† #1 Secondary photons from fluorescent scattering. Correction maximal directly above absorption edges, 0 directly below Zn edge. #2 Correction for bandwidth. Maximal at edge energies – 9.6667, 12.6631 keV. #3 Correction for monochromator drift. Maximal at 9.3298 keV. #4 Dark current correction and corresponding uncertainty (± 2 counts). #5 Standard errors from counting statistics (variance including precision and systematics). #6 Sum of relative uncertainties. #7 Absolute accuracy of the full-foil mapping technique. #8 Blank current correction and corresponding uncertainty. Correction maximal at low energies. #9 Error in the fit of the energy calibration data – minimum of 0.88 eV at 12.0503 keV, maximum of 1.22 eV at 9.5892 keV.

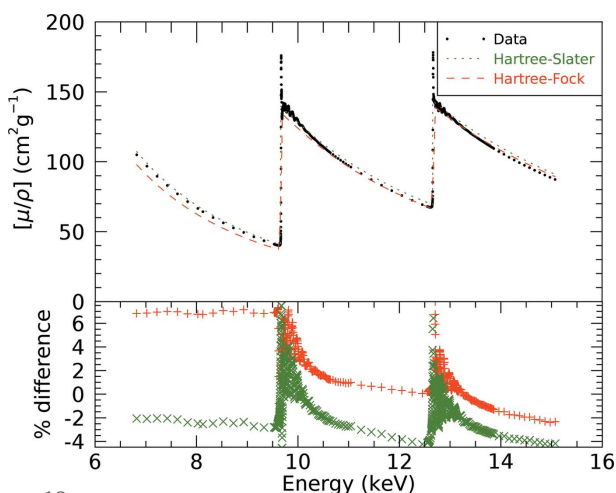


Figure 12
Comparisons of the experimental mass attenuation coefficient with Hartree–Slater (x) and Hartree–Fock (+) calculations.

normalized Hartree–Slater results [XCOM] over the Hartree–Fock renormalization. However, it must be remembered that this was not a full nor fully converged relativistic ansatz but only the renormalization of the coefficient by the Hartree–Fock versus Hartree–Slater amplitude at the nucleus. Conversely the more fully relativistic [DFT] prediction of FFAST is in general superior in this range without requiring a significant renormalization for density.

6.4. Error analysis and typical uncertainties in tables and supplementary information

Table 1 presents a summary of the key contributions to the uncertainty in the reported measurements, including the magnitude of the corrections for each systematic as well as the resultant uncertainty introduced. The table is broken into sections describing the absolute and relative uncertainty. Notice that the magnitude of the corrections for fluorescence (#1), bandwidth (#2) and dark current (#4) are very large and

located in particular regions of energy and data points so contribute explicitly to the relative shift and to pre-edge and XANES and XAFS structure. Notice also that the dark current correction is even very significant for a thin foil (25 μm) so should be routinely measured and corrected for, as with the other effects, especially since this drifts with time and environment at most synchrotron beamlines. The monochromator drift was a particular effect on this beamline and will be negligible on numerous other beamlines, and in this case mainly affected a few points. After correction the relative and absolute uncertainties are small. At different beamlines with much higher fluxes these can be even smaller after correction.

A table of the final results is in the supporting information. The supporting information also contains the data in template formats for .cif files and ifeffit-like eeffit.dat files for further portability and processing. We also include the extracted χ versus k spectra for both Zn and Se K -edges for comparison and fitting with different theoretical approaches.

7. Pre-analysis and FEFF8 analysis

The fine-structure function $\chi(k)$ was extracted from each of the absorption edges by using the *Mu2Chi* non-interpolation background subtraction software (Schalken & Chantler, 2018). By first finding the edge energy E_0 (Kraft *et al.*, 1996), fitting and then removing a spline, *Mu2Chi* returns the fine-structure function in k space,

$$k = \frac{2\pi}{h} [2m_e(E - E_0)]^{1/2}, \quad (28)$$

with fully propagated errors as seen in Fig. 13. *Mu2Chi* also has the capability to perform linear or cubic interpolations of the data.

Once obtained, the fine-structure function is used for subsequent nanostructural analysis, which proceeds by using output from *FEFF 8.1* XAFS simulation code (Ankudinov *et*

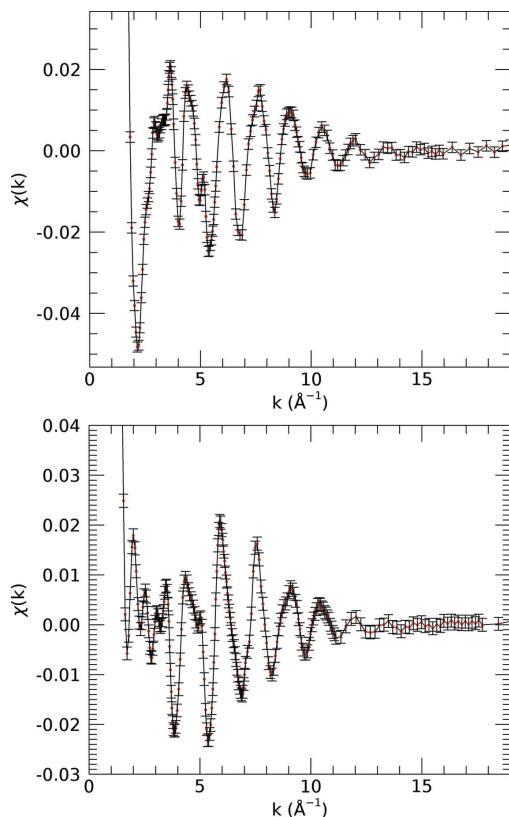


Figure 13
Fine-structure function for the (top) zinc and (bottom) selenium K -edges as output by *Mu2Chi* using edge energy determinations of 9667.11 eV and 12663.10 eV, respectively.

al., 1998) as input to the *eFEFFIT* computational package (Schalken & Chantler, 2018). The theoretical spectra are calculated using the photoelectron wave model (Lee & Pendry, 1975; Barton & Shirley, 1985*b*) and expressed as a sum of scattering paths through the XAFS equation (Zabinsky *et al.*, 1995),

$$\chi_{\text{th}}(k) = \sum_j N_j S_0^2 K_j(k) \frac{\sin[2kr_j + \phi(k)]}{kr_j^2} \times \exp(-2\sigma_j^2 k^2) \exp\left[\frac{2r_j}{\lambda_j(k)}\right], \quad (29)$$

where N_j is the degeneracy of the path, S_0^2 corresponds to many-body reduction effects, approximated as constant, $F_j(k)$ is the backscattering amplitude function, $\phi(k)$ is the phase shift, σ_j is the Debye–Waller factor for thermal motion, λ_j is the photoelectron mean free path, and $r_j = (1 + \alpha_j)r_{0,j}$ is the half path length, with α being the relative scaling due to thermal expansion. r_j in XAFS certainly involves local dynamic contributions from atomic motions.

eFEFFIT is based on the already well established *IFEFFIT* computational package (Newville, 2001). The benefit of *eFEFFIT* is that it enables experimental uncertainties to be input and propagated. These can then be used to determine the fit as well as the χ_r^2 goodness of fit statistic as defined by (Smale *et al.*, 2006)

$$\chi_r^2 = \frac{\chi^2}{N_{\text{pts}} - N_{\text{var}}}, \quad (30)$$

$$\chi^2 = \sum_{i=1}^{N_{\text{pts}}} \left[\frac{\chi_{\text{data}}(k_i) - \chi_{\text{theory}}(k_i)}{\sigma(k_i)} \right]^2, \quad (31)$$

where it is important to distinguish between χ as the fine structure function and χ the quality of the fit.

In the final analysis, 40 independent scattering paths were fitted to the data in χ versus k space between $k = 3.4 \text{ \AA}^{-1}$ and 18.9 \AA^{-1} . Below this range, the theory underpinning the fitting function begins to break down; above this range the data becomes sparse. The first two nearest-neighbour bond lengths were free parameters as these paths were determined to have the highest impact to the resultant fit. The results of the fit are presented in Fig. 14.

We tested a range of different fitting windows. In our analysis, propagating uncertainty from the raw data, the upper limit of the fitting range is usually arbitrary and has no influence as the uncertainties are getting larger and larger compared with the structure. However, the lower limit is potentially sensitive and depends in part on the limitations of

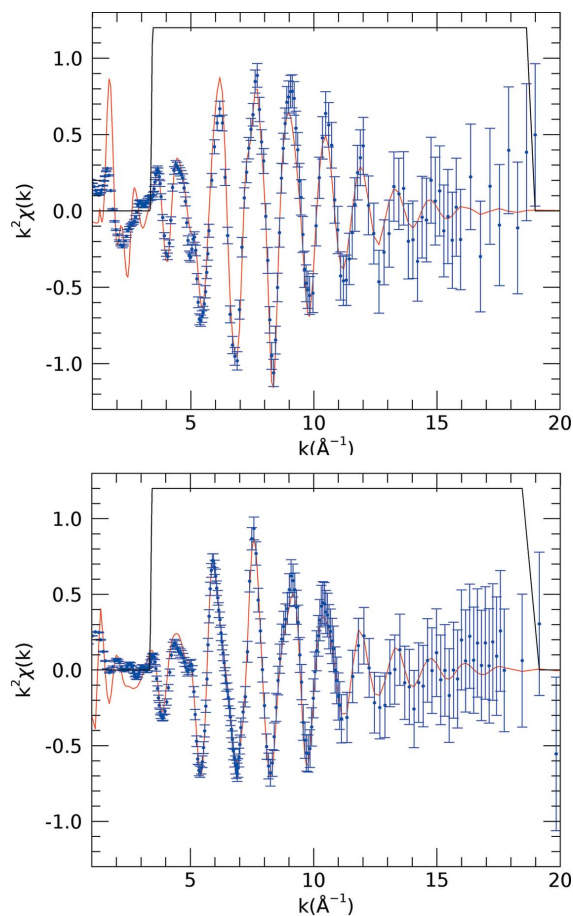


Figure 14
Fitted model output (red) with experimental data (blue) and uncertainties for the (top) zinc and (bottom) selenium K -edges. Also visible is the black box indicating the k Hanning window over which the data was fitted.

the theory and potential model structure. By reducing the lower bound of the Hanning window, χ_r^2 rises rapidly, and bond lengths can be distorted by 4%. Raising the lower bound significantly leads to less data to fit and a potential lowering of S_0^2 as the offset becomes ill-defined.

We performed a grid search on S_0^2 from 0.6 through 1.0 and fitted all other parameters at each point. The values at each edge should be similar. Note all other parameters are consistent. S_0^2 can be affected by the edge energy, separately the fitting offset E_0 , and also by limitations of the spline background subtraction. The accuracy of, for example, FEFF at low k also influences the determined value of S_0^2 . Since these depend upon the specific edge, they can and should vary somewhat from one edge to another. We report the 0.8 fit as this gave sensible parameters and was a reasonable minimum in plausible S_0^2 space. Fitted parameters are summarized in Table 2. σ^l values differ from the Zn edge analysis to the Se edge analysis by approximately 2σ . With the exception of this, the fits give very good physical agreement between both themselves and one another within 1σ . Comparison of the nearest neighbour (Zn–Se) bond length of 2.454 Å (Vèrié, 1997) determined by XRD, and 2.43 Å (Šipr *et al.*, 1997) determined by fitting XANES spectra using density functional theory, shows that our value is of order $0.77\% \pm 0.12\%$ and $1.8\% \pm 0.12\%$ larger for the Zn edge fit, respectively, and $0.66\% \pm 0.11\%$ and $1.7\% \pm 0.11\%$ larger for the Se edge fit.

An interesting result of this analysis is the different expansions obtained for the nearest and second nearest scattering paths. The scaling factor $\alpha = 1.0075$ for both edges represents an overall scaling of the lattice constant a . We obtain scaling factors for the nearest-neighbour scattering path of 1.0073 and 1.0062 for the zinc and selenium edge fits, respectively, with these both typically within 1σ of the overall scale α , hence in very good agreement. The second nearest-neighbour scattering paths, however, have consistent scalings of 1.012 and 1.011 for the zinc and selenium edges, respectively, and somewhat inconsistent with our previous expansion coefficients. Since XAFS is sensitive also to atomic vibrations perpendicular to the bond direction, a bond length 0.01 Å to 0.02 Å larger than XRD results at room temperature would be no surprise. These vibrations may also be responsible for the observed difference in scaling factors between first nearest and second nearest neighbours. This could suggest dynamic motion within the crystal lattice that is otherwise inaccessible by other techniques but will need further investigation.

We also observe edge jumps of $95.87 \text{ cm}^2 \text{ g}^{-1}$ and $77.98 \text{ cm}^2 \text{ g}^{-1}$ for the zinc and selenium edges, respectively, compared with values of $98.99 \text{ cm}^2 \text{ g}^{-1}$ and $74.25 \text{ cm}^2 \text{ g}^{-1}$ for XCOM tabulation and $100.75 \text{ cm}^2 \text{ g}^{-1}$ and $75.08 \text{ cm}^2 \text{ g}^{-1}$ from FFAST. These lead to leading to an edge ratio of Zn:background = 3.380:1 (3.334:1 and 3.466:1 for XCOM and FFAST, respectively) and Se:background = 2.153:1 (2.052:1 and 2.075:1 for XCOM and FFAST, respectively), before and after making allowance for Zn background and other shell background from FFAST.

Most other FEFF analyses of zinc selenide have been conducted on thin films, nanocrystalline samples and quantum

Table 2
eFEFFIT parameters for the fits of each edge.

Parameter	Zn edge		Se edge	
	Value	Error ($\pm 1\sigma$)	Value	Error ($\pm 1\sigma$)
S_0^2	0.915	0.041	0.8	–
$E_{0\text{cor}}$	6.20 eV	0.30 eV	6.33 eV	0.33 eV
Zn–Se	2.4728 Å	0.0029 Å	2.4701 Å	0.0032 Å
Zn–Zn†	4.0585 Å	0.0092 Å	–	–
Se–Se‡	–	–	4.053 Å	0.013 Å
α	1.0075	0.0022	1.0075	0.0023
σ^2 (Å ²)§	0.00739	0.00051	0.00959	0.00030
σ^2 (Å ²)¶	0.0189	0.0013	0.0225	0.0010
χ_r^2		3.54		3.24

† Second nearest neighbour bond length of Zn edge. ‡ Second nearest neighbour bond length of Se edge. § Only applied to nearest neighbour (shortest) scattering path. ¶ Applied to all other scattering paths.

dots (Valeev *et al.*, 2008; Campos *et al.*, 2005; Song *et al.*, 2010) or on dopants implanted within the lattice to achieve n-type conductivity (Akimoto *et al.*, 1996; Cooper *et al.*, 2015). All of these specifications have the potential to alter the atomic structure thus making them not directly comparable. Significantly narrower k windows were used in those datasets with significantly fewer data points, and χ_r^2 values are not reported.

8. Conclusion

We have directly quantified the key sources of systematic error inherent in measurements using synchrotron radiation using the XERT applied to the binary crystal ZnSe at room temperature. We have presented one of very few XAFS investigations of this compound and present the most accurate values of the mass attenuation coefficients of zinc selenide to date. We determine separately estimates of uncertainty for the absolute value of the mass attenuation coefficient, the determination of density, the determination of X-ray energies across the range of the experiment, the uncertainty of the extracted mass absorption (photoelectric) coefficient, and the relative XAFS uncertainty prior to interpolation, spline background removal and transformation to χ versus k axis for XAFS fitting with propagation of uncertainties.

The magnitudes of the correction for dark current are very large (3%–40%) as expected, even for thin foils; and the magnitude of the correction for blank normalization is even larger [up to 51% for the thin samples (25 μm) and up to 23% for the 100 μm foil], especially at lower energies, pointing to the need for these to be routine corrections. Note also that the corrections for thin samples are also large, and that they affect the scale and magnitude of extracted χ oscillations in the experimental data. The energy calibration is a good example of the insight using XRD to calibrate energies in an XAS measurement, especially relating to the need for multiple measurements over the range of the XAFS. Harmonics, monochromator stability and bandwidth are directly investigated and corrected for, which affect distinct regions of the low-energy, high-energy and pre-edge regions, respectively. Interestingly, the more one investigates the XAFS region in detail, the more one is drawn to need to apply crystallographic

techniques and understanding to resolve discrepancies and systematics.

The investigation of the TDS cross section is critical to the comparison with theory and is quite novel. Uncertainties are detailed in the tables.

By incorporating these errors into a modified version *eFEFFIT* of the XAFS simulation code *IFEFFIT*, we are able to propagate the errors from our XERT measurements to make sensitive fits and potential hypothesis testing, including searches for the effects of dynamical motion. Hence we demonstrate the importance of non-interpolation on the nanostructural analysis, enabling a far more robust investigation of nanostructure and the quality of interpreted structure.

These measurements significantly improve our knowledge of the mass attenuation coefficient and also provide a new benchmark for theoretically calculated values over a ranges of energies. This energy range includes regions of high physical significance such as the *K*-absorption edge and EXAFS region, allowing for critical testing of assumptions surrounding wavefunctions, the exchange potential, multipole matrix elements and critical solid state effects including inelastic mean free paths, inelastic and elastic scattering cross sections for materials, and bonding. Further work is required to investigate current theoretical and experimental anomalies in bonding, edge positions, XAFS and nanostructure.

Acknowledgements

The authors acknowledge L. F. Smale and N. A. Rae for their experimental and conceptual contributions to this work. They acknowledge the Australian National Beamline Facility and the Australian Synchrotron. We sincerely acknowledge and are very grateful for the long and faithful collaboration with Z. Barnea which drove the investigation of ZnSe to investigate some of these anomalies.

References

Akimoto, K., Ogawa, T., Maruyama, T. & Kitajima, Y. (1996). *J. Cryst. Growth*, **159**, 350–353.
 Ankudinov, A. L., Ravel, B., Rehr, J. J. & Conradson, S. D. (1998). *Phys. Rev. B*, **58**, 7565–7576.
 Babonneau, F., Doeff, S., Leoustic, A., Sanchez, C., Cartier, C. & Verdagner, M. (1988). *Inorg. Chem.* **27**, 3166–3172.
 Barnea, Z., Creagh, D. C., Davis, T. J., Garrett, R. F., Janky, S., Stevenson, A. W. & Wilkins, S. W. (1992). *Rev. Sci. Instrum.* **63**, 1069–1072.
 Barton, J. J. & Shirley, D. A. (1985a). *Phys. Rev. B*, **32**, 1892–1905.
 Barton, J. J. & Shirley, D. A. (1985b). *Phys. Rev. B*, **32**, 1906–1920.
 Beale, A. M. & Weckhuysen, B. M. (2010). *Phys. Chem. Chem. Phys.* **12**, 5562–5574.
 Bearden, J. A. & Burr, A. F. (1967). *Rev. Mod. Phys.* **39**, 125–142.
 Beer, A. (1852). *Ann. Phys. Chem.* **162**, 78–88.
 Berger, M. J. & Hubbell, J. H. (1987). *XCOM: Photon cross sections on a personal computer*. Technical Report. National Bureau of Standards, Washington, DC, USA.
 Booth, C. H. & Hu, Y. J. (2009). *J. Phys. Conf. Ser.* **190**, 012028.
 Bourke, J. D. & Chantler, C. T. (2012). *J. Phys. Chem. A*, **116**, 3202–3205.
 Bourke, J. D. & Chantler, C. T. (2014). *J. Electron Spectrosc. Relat. Phenom.* **196**, 142–145.

Brugger, J., Etschmann, B., Liu, W., Testemale, D., Hazemann, J.-L., Emerich, H., van Beek, W. & Proux, O. (2007). *Geochim. Cosmochim. Acta*, **71**, 4920–4941.
 Campos, C. E. M., Lima, J. C., Grandi, T. A., Itié, J. P., Polian, A. & Michalowicz, A. (2005). *J. Phys. Condens. Matter*, **17**, 5187–5200.
 Chandris, D., Magnan, H., Jezequel, G., Hricovini, K., Rossi, G., Villette, B. & Lecante, J. (1990). *Phys. Scr.* **T31**, 239–246.
 Chantler, C. T. (1995). *J. Phys. Chem. Ref. Data*, **24**, 71–643.
 Chantler, C. T. (2000). *J. Phys. Chem. Ref. Data*, **29**, 597–1056.
 Chantler, C. T. (2009). *Eur. Phys. J. Spec. Top.* **169**, 147–153.
 Chantler, C. T. & Barnea, Z. (1999). *J. Phys. Condens. Matter*, **11**, 4087–4091.
 Chantler, C. T., Barnea, Z., Tran, C. Q., Rae, N. A. & de Jonge, M. D. (2012). *J. Synchrotron Rad.* **19**, 851–862.
 Chantler, C. T., Barnea, Z., Tran, C. Q., Tiller, J. B. & Paterson, D. (1999). *Opt. Quantum Electron.* **31**, 495–505.
 Chantler, C. T., Islam, M. T., Best, S. P., Tantau, L. J., Tran, C. Q., Cheah, M. H. & Payne, A. T. (2015). *J. Synchrotron Rad.* **22**, 1008–1021.
 Chantler, C. T., Tran, C. Q., Paterson, D., Barnea, Z. & Cookson, D. J. (2000). *X-ray Spectrom.* **29**, 449–458.
 Chantler, C. T., Tran, C. Q., Paterson, D., Cookson, D. & Barnea, Z. (2001). *Phys. Lett. A*, **286**, 338–346.
 Chevallier, S., Réguerre, A.-L., Le Bail, A. & Della Valle, G. (2014). *Food. Biophys.* **9**, 219–228.
 Cookson, D. J. (1998). *J. Synchrotron Rad.* **5**, 1375–1382.
 Cooper, J. K., Gul, S., Lindley, S. A., Yano, J. & Zhang, J. Z. (2015). *Appl. Mater. Interfaces*, **7**, 10055–10066.
 Diop, D. & Grisenti, R. (1995). *Physica B*, **208–209**, 89–90.
 Fedorov, V. A., Ganshin, V. A. & Korkishko, Y. N. (1991). *Phys. Status Solidi A*, **126**, K5–K7.
 Filippini, A. (1995). *J. Phys. Condens. Matter*, **7**, 9343–9356.
 Freeman, D. K., Mair, S. L. & Barnea, Z. (1977). *Acta Cryst.* **A33**, 355–359.
 Fuwa, K. & Valle, B. L. (1963). *Anal. Chem.* **35**, 942–946.
 Gerward, L. (1992). *Nucl. Instrum. Methods Phys. Res. B*, **69**, 407–412.
 Gerward, L. & Thuesen, G. (1977). *Z. Naturforsch. A*, **32**, 588–593.
 Glover, J. L., Chantler, C. T., Barnea, Z., Rae, N. A. & Tran, C. Q. (2010). *J. Phys. B At. Mol. Opt. Phys.* **43**, 085001.
 Glover, J. L., Chantler, C. T., Barnea, Z., Rae, N. A., Tran, C. Q., Creagh, D. C., Paterson, D. & Dhal, B. (2008). *Phys. Rev. A*, **78**, 052902.
 Hester, J., Cookson, D., Garrett, R., Lane, S. & Hunter, B. (2020). *Python Powder Data Analyse Software for Extraction of Powder Diffraction Patterns from Image Plates*, <https://zenodo.org/record/3788753#Xyl9uRnTXOE>.
 Hildebrand, F. B. (1987). *Introduction to Numerical Analysis*. Courier Corporation.
 Huang, H. K. & Wu, S. C. (1976). *Comput. Biol. Med.* **6**, 337–343.
 Huang, M.-Z. & Ching, W. Y. (1993). *Phys. Rev. B*, **47**, 9449–9463.
 Indirajith, R., Rajalakshmi, M., Ramamurthi, K., Ahamed, M. B. & Gopalakrishnan, R. (2014). *Ferroelectrics*, **467**, 13–21.
 Iwanowski, R., Ławniczak-Jabłońska, K. & Traverse, A. (1997). *Acta Phys. Pol. A*, **91**, 803–808.
 Johnston, R. W. & Tomboulian, D. H. (1954). *Phys. Rev.* **94**, 1585–1589.
 Jonge, M. D. de, Barnea, Z., Tran, C. Q. & Chantler, C. T. (2004a). *Meas. Sci. Technol.* **15**, 1811–1822.
 Jonge, M. D. de, Barnea, Z., Tran, C. Q. & Chantler, C. T. (2004b). *Phys. Rev. A*, **69**, 022717.
 Jonge, M. D. de, Tran, C. Q., Chantler, C. T., Barnea, Z., Dhal, B. B., Cookson, D. J., Lee, W.-K. & Mashayekhi, A. (2005). *Phys. Rev. A*, **71**, 032702.
 Kikuma, I. & Furukoshi, M. (1985). *J. Cryst. Growth*, **71**, 136–140.
 Kincaid, B. M. & Eisenberger, P. (1975). *Phys. Rev. Lett.* **34**, 1361–1364.

- Kraft, S., Stümpel, J., Becker, P. & Kuetgens, U. (1996). *Rev. Sci. Instrum.* **67**, 681–687.
- Kwon, H.-T. & Park, C.-M. (2014). *J. Power Sources*, **251**, 319–324.
- Ladeira, A. C. Q., Ciminelli, V. S. T., Duarte, H. A., Alves, M. C. M. & Ramos, A. Y. (2001). *Geochim. Cosmochim. Acta*, **65**, 1211–1217.
- Lee, P. A. & Pendry, J. B. (1975). *Phys. Rev. B*, **11**, 2795–2811.
- Mair, S. L., Prager, P. R. & Barnea, Z. (1971). *Nat. Phys. Sci.* **234**, 35.
- Mathey, Y., Mercier, H., Michalowicz, A. & Leblanc, A. (1985). *J. Phys. Chem. Solids*, **46**, 1025–1029.
- McIntyre, G. J., Moss, G. & Barnea, Z. (1980). *Acta Cryst.* **A36**, 482–490.
- Neidig, M. L., Sharma, J., Yeh, H.-C., Martinez, J. S., Conradson, S. D. & Shreve, A. P. (2011). *J. Am. Chem. Soc.* **133**, 11837–11839.
- Newville, M. (2001). *J. Synchrotron Rad.* **8**, 322–324.
- Newville, M. (2016). *XAFS Spectra Library (beta) – Spectrum: ZnSe (RT)*, <https://cars.uchicago.edu/xaslib/spectrum/616>.
- Nordfors, B. (1960). *Ark. Fys.* **18**, 37–47.
- Perkins, S. T., Cullen, D. E., Chen, M. H., Hubbell, J. H., Rathkopf, J. & Scofield, J. H. (1991). Lawrence Livermore Laboratory Report UCRL-50400, EADL Z = 1–100. Technical Report Lawrence Livermore Laboratory Report. Lawrence Livermore National Laboratory, California, USA.
- Rehr, J. J. & Albers, R. C. (2000). *Rev. Mod. Phys.* **72**, 621–654.
- Rehr, J. J. & Ankudinov, A. L. (2005). *Coord. Chem. Rev.* **249**, 131–140.
- Saloman, E. & Hubbell, J. (1987). *Nucl. Instrum. Methods Phys. Res. A*, **255**, 38–42.
- Sano, H., Ohtaka, K. & Ohtsuki, Y.-H. (1969). *J. Phys. Soc. Jpn*, **27**, 1254–1261.
- Sarode, P. R., Ramasesha, S., Madhusudan, W. H. & Rao, C. N. R. (1979). *J. Phys. C. Solid State Phys.* **12**, 2439–2445.
- Schalken, M. J. & Chantler, C. T. (2018). *J. Synchrotron Rad.* **25**, 920–934.
- Scofield, J. H. (1973). Lawrence Livermore Laboratory Report UCRL-51326. Lawrence Livermore National Laboratory, California, USA.
- Scofield, J. H. (1974). *Atom. Data Nucl. Data Tables*, **14**, 121–137.
- Šipr, O., Machek, P., Šimůnek, A., Vackář, J. & Horák, J. (1997). *Phys. Rev. B*, **56**, 13151–13161.
- Smale, L. F., Chantler, C. T., de Jonge, M. D., Barnea, Z. & Tran, C. Q. (2006). *Radiat. Phys. Chem.* **75**, 1559–1563.
- Song, J., Zhang, J., Xie, Z., Wei, S., Pan, Z., Hu, T. & Xie, Y. (2010). *Nucl. Instrum. Methods Phys. Res. A*, **619**, 280–282.
- Sritharan, S., Jones, K. A. & Motyl, K. M. (1984). *J. Cryst. Growth*, **68**, 656–664.
- Stern, E. A. (1974). *Phys. Rev. B*, **10**, 3027–3037.
- Stevenson, A. W. & Barnea, Z. (1983a). *Acta Cryst.* **A39**, 538–547.
- Stevenson, A. W. & Barnea, Z. (1983b). *Acta Cryst.* **A39**, 548–552.
- Su, C.-H., Feth, S. & Lehoczky, S. L. (2009). *Mater. Lett.* **63**, 1475–1477.
- Swinehart, D. F. (1962). *J. Chem. Educ.* **39**, 333.
- Tantau, L. J., Chantler, C. T., Bourke, J. D., Islam, M. T., Payne, A. T., Rae, N. A. & Tran, C. Q. (2015). *J. Phys. Condens. Matter*, **27**, 266301.
- Tran, C. Q., Barnea, Z., de Jonge, M. D., Dhal, B. B., Paterson, D., Cookson, D. J. & Chantler, C. T. (2003b). *X-ray Spectrom.* **32**, 69–74.
- Tran, C. Q., Chantler, C. T. & Barnea, Z. (2003c). *Phys. Rev. Lett.* **90**, 257401.
- Tran, C. Q., Chantler, C. T., Barnea, Z., Jonge, M. D., Dhal, B. B., Chung, C. T. Y., Paterson, D. & Wang, J. (2005). *J. Phys. B At. Mol. Opt. Phys.* **38**, 89–107.
- Tran, C. Q., Chantler, C. T., Barnea, Z., Paterson, D. & Cookson, D. J. (2003a). *Phys. Rev. A*, **67**, 042716.
- Tran, C. Q., Jonge, M. D., Barnea, Z. & Chantler, C. T. (2004). *J. Phys. B At. Mol. Opt. Phys.* **37**, 3163–3176.
- Triboulet, R., Ndap, J., El Mokri, A., Carli, A. T. & Zozime, A. (1995). *J. Phys. IV*, **5**(C3), 141–149.
- Valeev, R. G., Deev, A. N., Gilmutdinov, F. Z., Bystrov, S. G., Pivovarova, O. I., Romanov, A., Kriventsov, V. V., Sharafutdinov, M. R. & Eliseev, A. A. (2008). *J. Struct. Chem.* **49**, 124–128.
- Vèrié, C. (1997). *Mater. Sci. Eng. B*, **43**, 60–64.
- Vishnoi, A. N. & Agarwal, B. K. (1969). *Phys. Lett. A*, **29**, 105–106.
- Waychunas, G. A., Rea, B. A., Fuller, C. C. & Davis, J. A. (1993). *Geochim. Cosmochim. Acta*, **57**, 2251–2269.
- Wilson, A. J. C. & Geist, V. (1993). *Cryst. Res. Technol.* **28**, 110.
- Wyckoff, R. W. G. (1963). *Crystal Structures*, Vol. 1, p. 15. New York: Interscience.
- Yang, X., Yang, Q., Hu, Z., Zhang, W., Li, H., Li, L., Qiu, Y., Xu, N., Wu, J. & Sun, J. (2016). *RSC Adv.* **6**, 98413–98421.
- Zabinsky, S. I., Rehr, J. J., Ankudinov, A., Albers, R. C. & Eller, M. J. (1995). *Phys. Rev. B*, **52**, 2995–3009.